A Light Field FDL-HCGH Feature in Scale-Disparity Space

Meng Zhang, Haiyan Jin, Zhaolin Xiao, Christine Guillemot

A Light Field FDL-HCGH Feature in Scale-Disparity Space

Meng Zhang*, Haiyan Jin*, Zhaolin Xiao*, and Christine Guillemot† (IEEE Fellow)

***Abstract*—Many computer vision applications rely on feature detection and description, hence the need for computationally efficient and robust 4D light field (LF) feature detectors and descriptors. In this paper, we propose a novel light field feature descriptor based on the Fourier disparity layer representation, for light field imaging applications. After the Harris feature detection in a scale-disparity space, the proposed feature descriptor is then extracted using a circular neighborhood rather than a square neighborhood. It is shown to yield more accurate feature matching, compared with the LiFF LF feature, with a lower computational complexity. In order to evaluate the feature matching performance with the proposed descriptor, we generated a synthetic stereo LF dataset with ground truth matching points. Experimental results with synthetic and real-world dataset show that our solution outperforms existing methods in terms of both feature detection robustness and feature matching accuracy.**

***Index Terms*—Light field, Fourier disparity layer, Feature detection, Feature description.**

I. Introduction

MANY computer vision applications heavily rely on image feature detection, description and matching. Image feature detection refers to the problem of identifying and localizing interest points, blobs and regions. Classic 2D image feature detection methods include Harris [1], SIFT [2], SURF [3], FAST [4], ORB [5], LBP [6], PCA-SIFT [7], GLOH [8], etc. These methods have been widely employed in various computer vision applications, such as target tracking, 3D reconstruction and industry inspection etc [9], [10]. These feature detectors are mainly based on specific image gradient distributions, which have local or global invariance to possible image translation, rotation, or to scale or affine transformation. Therefore, the identifiability and invariance of features description are critical in feature matching. For instance, the SIFT feature [2] is widely used because of its invariance to rotation and scale transformations. However, the matching precision and robustness with 2D image features remains a difficult problem in presence of occlusions, non-Lambertian surfaces, illumination changes etc.

In order to overcome limitations of 2D image features, higher dimensional data such as 3D point cloud [11], RGB-D images [12], [13], and 4D light fields, [14], [15] have been considered in object recognition and tracking applications. Features extracted from higher dimensional data have shown a great potential for improving both matching accuracy and robustness. For example, the authors in [11], [16] and [17] introduce methods for extracting features from 3D point cloud data in order to have a more precise 3D object modeling and recognition. Gao *et al*. [13] propose a planar point feature detection for improving the reconstruction precision of a RGB-D SLAM system, in presence of noise. Gupta *et al*. [18] suggest to encode height above ground and angle with gravity information for each pixel of RGB-D images, which enables more accurate object detection and semantic segmentation than only using raw depth images. However, 3D point clouds and RGB-D images still do not preserve the incident light rays orientation, which can bring useful information for 3D object recognition and reconstruction in particular in presence of occlusions and non-Lambertian surfaces.

Light fields, unlike 2D images and RGB-D images, by recording the flow of rays emitted by the scene along different directions, yield a 4D spatio-angular representation of the scene, from which one can extract information about the parallax and depth of the scene. 4D LF features therefore hold promises to solve limitations of 2D image features in presence of occlusions and non-Lambertian scenes. This is investigated in [19] and [14] where the authors exploit depth information in the LF to build scale-depth descriptors. Another category of approaches builds upon 2D descriptors, by computing 2D detectors on the different sub-aperture images, and then imposing angular consistency using epipolar geometry [20], [21] or using optical flows [22], [23]. The authors in [15] instead simultaneously consider all sub-aperture images and extend the SIFT descriptor to 4D LF by searching for features in a joint 4D scale-slope space. More precisely, the feature called LIFF proposed in [15] is computed in the scale space like SIFT, but at different depths, or for different slopes of structures in epipolar plane images (EPI).

LF features have already been considered for a variety of applications. Ghasemi *et al*. [19] propose a scale-invariant feature vector computed by applying a Hough or Radon transformation to epipolar plane images, for fast and accurate building scene classification. Raghavendra *et al*. [24] propose a face presentation attack detection by exploring the feature variation of the focus between multiple depth (or focus) images. Tsai *et al*. [25] instead proposed a method to distinguish between refracted and Lambertian image features using a LF camera, based on textural cross-correlation to characterize apparent feature motion across the LF. Ji *et al*. [26] propose a LF directional gradient histogram (LFHoG) feature to achieve

* Xi'an University of Technology, Xi'an 710048, China.
† Institut National de Recherche en Informatique et en Automatique (INRIA), Rennes 35000, France.
Corresponding author: Zhaolin Xiao, email:xiaozhaolin@xaut.edu.cn. This work has been funded in part by the National Natural Science Foundation of China (No. 61871319 and No. 62031023), and in part by the EU H2020 Research and Innovation Programme under grant agreement No 694122 (ERC advanced grant CLIM).
Manuscript received xxx xx, 2021.

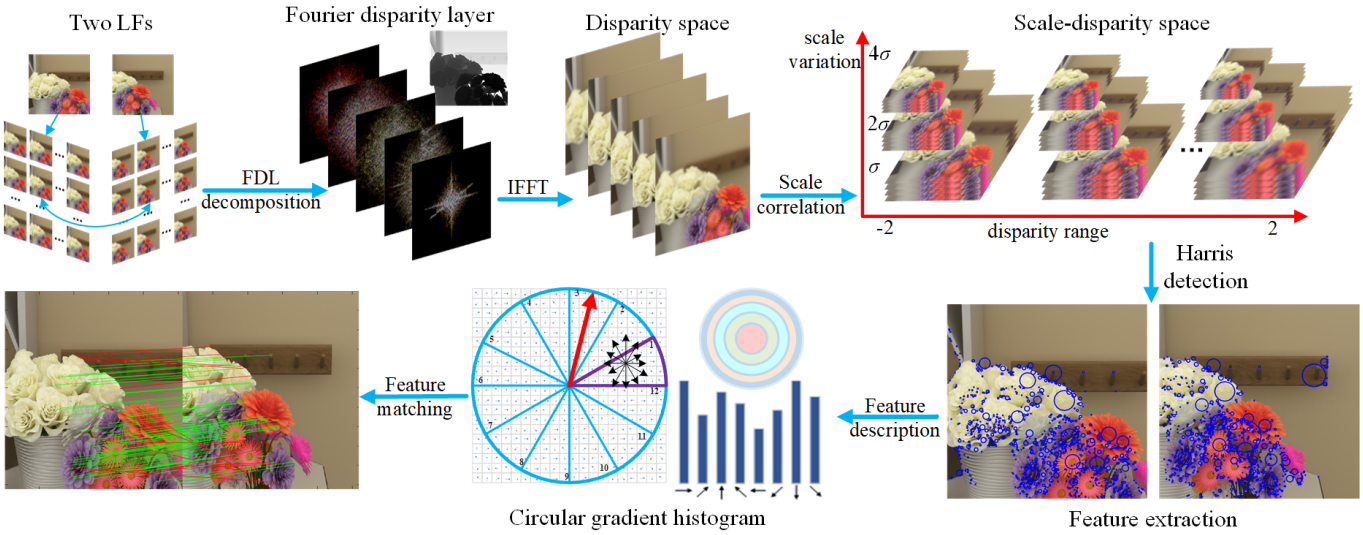

Fig. 1. Overview of FDL-HCGH feature matching. The LF pairs are first converted into Scale-disparity space using FDL decomposition. Then, the feature points are extracted by Harris detector, and are quantified with the proposed CGH based descriptor. The proposed FDL-HCGH feature matching outperforms the state-of-art algorithms in terms of matching precision and computational complexity.

high precision live face detection, while a LF local binary patterns (LFLBP) is introduced in [27], which enhances the LF based face recognition. The authors in [28] propose a solution of accurate and fast disparity estimation by introducing a binary descriptor, which exploits the light field gradient over both the spatial and the angular dimensions.

Despite the above work, defining robust and computationally efficient 4D LF feature extractors and descriptors is still a widely open problem. One question inherent to the LiFF feature [15] is the discretization of the depth space, which has obvious implications on computational complexity. The depth space discretization corresponds to a finite list of possible slope values for the EPI line structures. A higher number of slope values gives a better performance, but a higher computational complexity. The optimal list of slope values is not easy to determine. The authors recommend using as many slopes as there are samples in the LF angular dimension.

In this paper, we propose a novel 4D LF feature, called FDL-HCGH feature, based on the multi-scale Harris detector and circular gradient histogram descriptor computed on the Fourier disparity layer representation [29]. The Fourier disparity layer (FDL) is a compact representation, which samples the LF in the depth (or equivalently the disparity) dimension by decomposing the scene as a discrete sum of layers. The proposed feature is therefore defined in the 4D LF scale-disparity space, the disparity being discretized thanks to the FDL construction. This compact representation leads to a reduced computational complexity without loosing in terms of performance.

We then propose a new descriptor that extends the descriptor we introduced in [30] by replacing the SIFT-like descriptor with a novel circular gradient histogram (CGH) based descriptor, exploiting the scale-disparity space constructed using the FDL-based LF representation [29]. We consider both an annular gradient histogram (AGH) and a sector gradient histogram (SGH). The annular gradient and sector gradient histograms are both referred to as circular gradient histograms (CGH). Note that a sector-ring histogram of gradients has already been considered in [31] for rotation-invariant human detection. However, here, the Harris detector and the CGH descriptor are combined in the FDL domain to form a novel FDL-HCGH feature, the performance of which outperforms [30] in terms of both precision and computational complexity. We show an overview of the proposed FDL-HCGH feature in figure 1. The contributions of this work can be summarized as follows:

- We introduce a light field descriptor based on circular gradient histograms computed on the FDL light field representation. This descriptor is shown to greatly improve the precision of feature matching compared with the classic SIFT and LiFF [15] descriptors.
- By combining the Harris detector and the CGH descriptor, the computational complexity is significantly reduced compared with LiFF [15] and FDL-HSIFT [30].
- We extended the feature matching dataset [1] of [30] to real-world scenes, so that the proposed feature can be evaluated in presence of real noise.

II. FDL-HCGH Feature Detection and Description

A. Light field parameterization

A light field, as proposed in [32] and [33], can be represented by a 4D function $LF(x, y, u, v)$ which describes the radiance along light rays. This representation is based on the parameterization of the radiance along rays by their intersection with two-parallel-planes, with the parameters (x, y) and (u, v) describing the intersection points of the ray with the two planes. The pairs (x, y) and (u, v) represent the spatial and angular coordinates of light rays respectively. In the past two decades, many acquisition devices have been designed

[1]Both the synthetic and real-world LF matching dataset can be downloaded from https://github.com/MengZhang-XAUT/light-field-matching-datasets

to capture LF, ranging from camera arrays [34], to single cameras mounted on moving gantries, and plenoptic cameras [35]. Overviews of these devices can be found in [36], [37].

B. Construction of FDL-based scale-disparity space

1) Fourier disparity layer representation of Light fields: A 4D LF can be represented by a set of layers, each one corresponding to a different disparity value, and computed using a regularized least square regression in the frequency domain, hence the name Fourier Disparity Layers (FDL).

For simplicity of notation, let us consider only one 2D slice of the LF with only one spatial and one angular dimension. We assume that the scene is Lambertian, without occlusions, and that the scene can be divided into K spatial regions Ω_k with constant disparity $\{d_k\}_{k\in[1,K]}$. The Fourier transform of the LF can be computed as [29].

$$\hat{L}(w_x, w_u) = \sum_k \delta(w_u - d_k w_x)\hat{L}^k(w_x) \tag{1}$$

where w_x and w_u are spatial and angular frequencies. $\delta(w_u - d_k w_x)$ is a Dirac delta function, which simulates the aperture function with infinitely small aperture size. Each function $\hat{L}^k$ can be derived as,

$$\hat{L}^k(w_x) = \int_{\Omega_k} e^{-2i\pi x w_x} L(x,0)dx \tag{2}$$

and interpreted as the Fourier transform of the central view $L(x,0)$ only considering a spatial region Ω_k of disparity d_k. More generally, the Fourier Transform $\hat{L}_{u_0}$ of L_{u_0} (a LF view at angular coordinate u_0 defined by $L_{u_0}(x) = L(x,u_0)$), given a set of K disparity values $\{d_k\}_{k\in[1,K]}$, can be decomposed as [29]

$$\hat{L}_{u_0}(\omega_x) = \sum_k e^{+2i\pi u_0 d_k \omega_x}\hat{L}^k(\omega_x) \tag{3}$$

The FDL representation is therefore composed of the set of layers $\{L^k(x)\}$ (for a 2D slice) which can be derived from the inverse Fourier transform of $\hat{L}^k(w_x)$. The FDL representation is constructed using linear regression which automatically finds the correct discretization in the depth or disparity space, leading to a more compact representation, compared to a focal stack. The FDL representation has been shown efficient for various processing applications, e.g., rendering, view synthesis or varying aperture size and shape.

Note that, although the FDL model design principles are first introduced in [29], by assuming that the scene is Lambertian, without occlusions, a relaxation of the FDL model construction is also proposed in [29] in order to better cope with these limitations, and to allow a better representation of non-Lambertian effects and occlusions. The proposed light field descriptor constructed from this generalized FDL model will hence naturally benefit from its capacity to handle non-Lambertian surfaces and occlusions.

2) Construction of scale-disparity space: The FDL representation with the 3D notation, i.e., the set of layers $\{L^k(x,y)\}$, is derived by computing the inverse Fourier transform of $\hat{L}^k(w_x, w_y)$, as

$$L^k(x,y) = \iint \hat{L}^k(w_x, w_y)\mathrm{d}w_x\mathrm{d}w_y \tag{4}$$

Therefore, the different layers of the FDL representation define a discretization of the disparity space. Figure 2 shows an example of disparity space with 3 different disparity layers.

Fig. 2. Disparity space and corresponding Fourier disparity layer representation. The magnitude spectrum of each layer is shown in the red box.

Assuming that the features of an object only exist over a certain scale range [38], a multi-scale representation is constructed using a Gaussian kernel. To ensure that the proposed feature is robust to scale variations, we construct a scale-disparity space (SDS), as

$$\Psi^{k,\sigma}(x,y) = L^k(x,y) \bigotimes G(x,y,\sigma) \tag{5}$$

where $G(\cdot)$ is a Gaussian kernel function used to vary the scale. We construct the representation $\Psi^{k,\sigma}(x,y)$ in the SDS for each given input LF, and for a given number K of disparity layers and scale factor σ. For each FDL-layer, we construct a multi-scale representation by using Equation (5). Specifically, suppose the initial scale is σ_0, the discretization of a continuous scale can be derived as

$$\sigma(o_i, s_j) = 2^{o_i + s_j/3}\sigma_0 \tag{6}$$

where o_i is the i-th octave, and s_j is the j-th slice in the current octave according to [38]. In this paper, both the number of octaves and the number of slices in each octave are set to 3, *i.e.*, $O = \{o_i | i = 1,2,3\}$, and $S = \{s_j | j = 1,2,3\}$. As in [38], the initial scale factor $\sigma_0 = 1.6$.

Let Ψ_L be the set of all possible $\Psi^{k,\sigma}$ of the left LF, and Ψ_R be the corresponding one of the right LF. In the SDS space, considering a specific feature point (x_0, y_0), it will be only valid on a subset of K disparity layers. This means that the feature point (x_0, y_0) is located only on the disparity layers where the object resides. As a result, the FDL-based space partitioning can filter out a large number of matching candidates that do not belong to the object. The feature points matching will only involve a subset of both Ψ_L and Ψ_R (indexed by k in $\Psi^{k,\sigma}$), which are marked as the blue boxes in the figure 3. Therefore, the computational complexity and false correspondences can be reduced by narrowing the set of matching candidates. Another reason for the computational complexity being lower than [15] is that, the FDL representation usually needs less layers than the number of images in a focal stack. As shown in figure 3, to enhance both matching robustness and precision, we conduct a cross scale-disparity features matching to deal with variations in scale and depth.

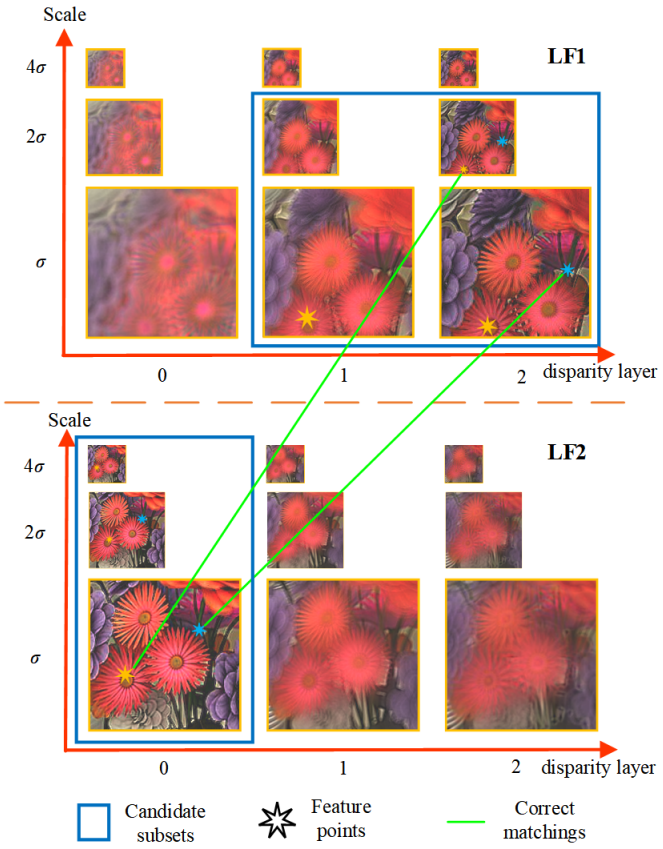

Fig. 3. Cross layer feature matching of two different LFs in the scale-disparity space. For example, the green lines are showing two pairs of correspondences that have been matched in different disparity layers (horizontal axis) and different scales (vertical axis).

C. FDL-HCGH feature detection

To ensure rapidity and sensitivity of the proposed FDL-HCGH feature detection, we use a Harris detector [1] in the SDS representation. Let $\Psi^{k,\sigma}(x,y)$ be a layer corresponding to the disparity d_k in the scale corresponding to the σ value, and (x,y) represent a pixel in the layer $\Psi^{k,\sigma}(x,y)$. Then, a displacement $(\Delta x, \Delta y)$ in the spatial dimension of the SDS can be represented as

$$\Psi^{k,\sigma}(\Delta x,\Delta y)=\sum_{x,y}\eta(x,y)[\Psi^{k,\sigma}(x+\Delta x,y+\Delta y) -\Psi^{k,\sigma}(x,y)]^2 \tag{7}$$

where $\eta(x,y)$ is a window function. By applying the Taylor expansion to Equation (7), the displacement can be derived as,

$$\begin{aligned}\Psi^{k,\sigma}(\Delta x,\Delta y)&=\sum_{x,y}\eta(x,y)[\Psi_x\Delta x+\Psi_y\Delta y]^2\\&=[\Delta x,\Delta y]\sum_{x,y}\eta(x,y)\begin{bmatrix}\Psi_x^2 & \Psi_x\Psi_y\\ \Psi_x\Psi_y & \Psi_y^2\end{bmatrix}\begin{bmatrix}\Delta x\\ \Delta y\end{bmatrix}\end{aligned} \tag{8}$$

where Ψ_x and Ψ_y are 1st-order partial derivatives of Ψ in the x and y directions respectively. The matrix M is the Harris matrix or structure tensor, which is defined as

$$M=\sum_{x,y}\eta(x,y)\begin{bmatrix}\Psi_x^2 & \Psi_x\Psi_y\\ \Psi_x\Psi_y & \Psi_y^2\end{bmatrix}=\begin{bmatrix}A & C\\ C & B\end{bmatrix} \tag{9}$$

By following [1], we compute the response function $R(x,y)$ at each pixel of coordinates (x,y) as

$$R(x,y)=det(M)-\lambda\cdot Tr^2(M) \tag{10}$$

where λ is the empirical coefficient within $[0.04, 0.06]$. By calculating the relation between the determinant and trace of the matrix M, the calculation of the response $R(x,y)$ avoids the computation of the eigenvalues of the matrix M, which is usually a computationally expensive process. To keep the sensitivity of the feature detection, we simply select the top percentages of the maximum response of each possible $\Psi^{k,\sigma}$ in the SDS space. Therefore, our detection will produce more feature points than LiFF [15], which detects the SIFT feature on the focal stack. Another advantage of the proposed detector is its robustness to scale variations. With a variable σ, the detected feature points are distributed on different scales, which enables cross-scale feature matching.

D. Feature description and matching

The SIFT feature descriptor proposed in [2], and based on gradients along different orientations, has been widely used in computer vision applications due to its invariance to rotation, translation and scale transformation. However, it suffers from a pretty high computational complexity. Its computation proceeds in two steps: feature main direction calculation and correction, feature descriptor generation. Firstly, the gradient magnitude and orientation of all pixels in the neighborhood of the feature are calculated and counted as a gradient histogram, in which the direction with the largest gradient magnitude corresponds to the main direction of the feature. The coordinate axis of the feature neighborhood is then rotated to be consistent with the main direction of the feature to ensure invariance to rotation. Then, a feature neighborhood is selected, and the gradient magnitude and orientation of pixels in the feature neighborhood are calculated again to generate feature descriptors. We propose using a circular neighborhood rather than a square neighborhood, and to compute an annular gradient histogram (AGH) and a sector gradient histogram (SGH). The annular gradient and sector gradient histograms are both referred to as circular gradient histograms (CGH) in the sequel.

1) Annular gradient histogram computation: We divide the feature neighborhood into five annular regions (see in figure 4), each annular region having the same area, i.e., the same number of pixels. Then, we calculate a gradient histogram with 18 bins in each annular region, i.e., covering the 360 degrees. The calculation of the gradient histogram includes the computation of the gradient magnitude $m(x,y)$ and the orientation $\theta(x,y)$ as

$$\begin{aligned}m(x,y)&=\sqrt{(Dx)^2+(Dy)^2}\\ \theta(x,y)&=arctan\frac{Dy}{Dx}\end{aligned} \tag{11}$$

in which,

$$\begin{aligned}Dx&=\Psi^{k,\sigma}(x+1,y)-\Psi^{k,\sigma}(x-1,y)\\ Dy&=\Psi^{k,\sigma}(x,y+1)-\Psi^{k,\sigma}(x,y-1)\end{aligned} \tag{12}$$

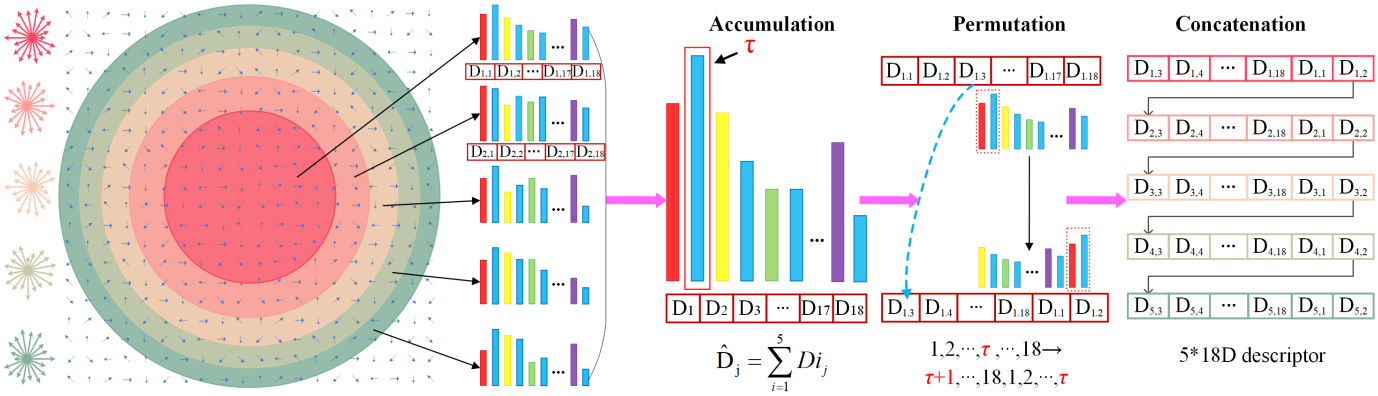

Fig. 4. Feature descriptor based on the annular gradient histogram. The feature neighborhood is divided into five annular regions with the same area. We calculate a gradient histogram on each annular region. The color of the annular region corresponds to the gradient histogram on the right. The gradient histograms of the five annular regions are permuted to align the dominant orientation of the feature with the coordinate axes, to ensure rotation invariance.

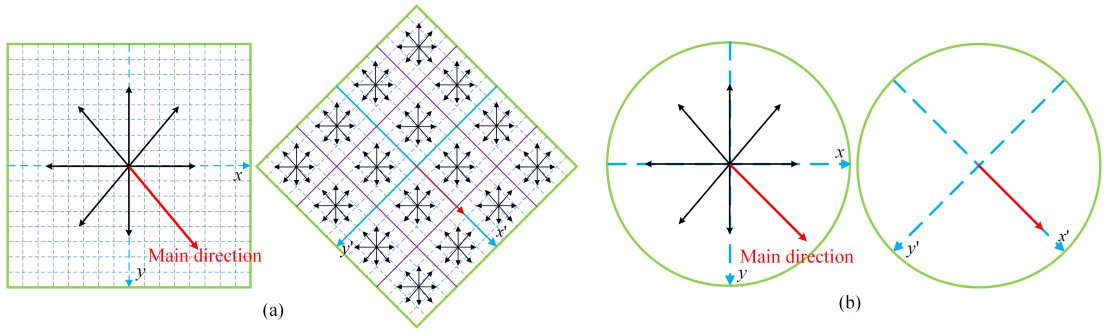

Fig. 5. Comparison of feature description between square neighborhood and circular neighborhood. (a) Feature description of square neighborhood; (b) Feature description of circular neighborhood.

As shown in figure 4, the gradient histograms in the five annular regions are denoted $\{D_{i,j}|i \in [1,5], j \in [1,18]\}$ where i represents the index of the annular region and j represents the index of the bins in the gradient histogram. In order to ensure rotation invariance of the feature descriptors, it is necessary to calculate the dominant direction τ of the feature neighborhood, that is, the direction of the peak of the gradient. The gradient histograms of five annular regions are multiplied by weights and accumulated to generate the gradient histograms of the whole feature neighborhood, as shown in figure 4(middle). The weights of the five annular regions are empirically set to $[0.5, 0.2, 0.1, 0.1, 0.1]$ from inside to outside. The closer the annular region to the feature point, the greater the influence on the feature descriptor. Then, the gradient histograms of the five annular regions are permuted to align the dominant orientation of the feature with the coordinate axes, to ensure rotation invariance. Finally, the feature histograms of the five annular regions are concatenated from the inside area to the outside area to construct a $5*18D$ feature descriptor, as shown in figure 4(right).

For a single $\Psi^{k,\sigma}(x,y)$, the $90D$ descriptor $f(\Psi^{k,\sigma}(x,y))$ consists of 5 annular regions with 18 directions in each. In this way, we calculate the descriptor $F(x,y)$ from an annular neighborhood with the radius of 11 pixels. $F(x,y)$ can be represented as

$$F(x,y) = \{f|f(\Psi^{k,\sigma}(x,y)), (k,\sigma) \in SDS\} \quad (13)$$

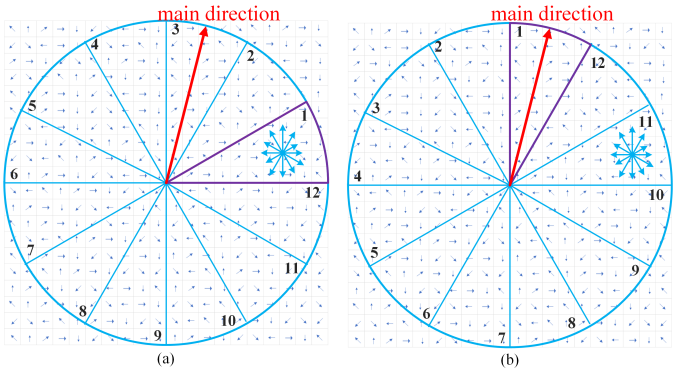

Fig. 6. Sector gradient histogram. (a) The feature neighborhood is divided into 12 sector regions, and on each sector region we calculate a gradient histogram. (b) The red arrow represents the main direction of the feature, and the index of the sector corresponding to the main direction is set to 1.

2) Sector gradient histogram: As shown in figure 6, we propose a feature descriptor based on the sector gradient histogram (SGH) and a circular neighborhood. Different from the AGH descriptor, in SGH descriptor, the circular feature neighborhood is evenly divided into 12 sector regions, each with an angle of 30 degrees, and the sector regions are numbered according to the order shown in figure 6(a). Equations (11) and (12) are used to calculate a gradient histogram with 12 bins in each sector region. Then, the gradient histograms of the 12 sector regions are concatenated to obtain the gradient

histogram of the whole circular feature neighborhood, in which the bin with the largest gradient magnitude corresponds to the main feature direction. For the $12 * 12D$ SGH descriptor, its sector division makes it easier to describe the changing structure in the circumferential direction. It ignores the the weights of gradient that vary along the radius of the circle, which is important in the AGH descriptor.

Figure 5 shows the difference between the SIFT and the CGH feature descriptors. As shown in figure 5(a) and 5(b), the SIFT feature neighborhood is square, and the pixels in the feature neighborhood change when aligning the dominant feature direction with the coordinate axes. So it is necessary to calculate the gradient histogram of the feature neighborhood twice. In contrast, to compute both the AGH and SGH descriptors, we need to calculate the gradient histogram of the feature neighborhood only once. With the AGH descriptor we perform the main direction alignment by shifting the feature descriptors of the five annular regions, while with the SGH descriptor we simply update the indices of the sector regions (hence of the local histograms, as shown in figure 6).

3) The distance metric in feature matching: To compute FDL-HCGH feature based matches, we measure the distance $\langle f_1(p), f_2(q) \rangle$ between two feature vectors at two pixel positions in LF_1 and LF_2 respectively, using a cosine based metric. The variables p and q denote the candidate matching coordinates in the candidate sets of two different LFs, *i.e.*F_1 and F_2. This distance can be expressed as

$$dist(p,q) = \max_{(k_1,\sigma_1),(k_2,\sigma_2)} (cos(f_1^{k_1,\sigma_1}(p), f_2^{k_2,\sigma_2}(q))), \quad \text{where} \quad f_1 \in F_1, f_2 \in F_2 \tag{14}$$

Since the feature correspondence is searched across different scales and disparity layers, it may lead one-to-multiple mapping from F_1 to F_2. Therefore, we take only the maximum matching for each $f_1 \in F_1$. To ensure the significance of features, we take the final matching decision by using a principal curvature ratio $r = dist(p, q_{max})/dist(p, q_{2nd})$. It is a positive matching only when $r < 0.75$, which means that the distance p to the nearest point q_{max} is clearly less than the distance p to the second nearest point q_{2nd}. In the experiments, we set the number of FDL layers $k = 9$ and use 3 scale level ($\sigma_0 = 1.6$). These parameter settings may need to be adjusted for complex scene with large disparities. For clarity, We summarize the FDL-HCGH feature detection and matching algorithm in Algorithm 1.

Algorithm 1 FDL-HCGH matching algorithm

Input: LF_1, LF_2.

Output: Matching point set $(p_1, p_2)|p_1 \in LF_1, P_2 \in LF_2$.

```
Construct the FDL of each LF (LF_1 and LF_2) by inverse Fourier transform of Equation (3);
Construct the SDS Ψ_n^{(k,σ)}(x, y) for each LF indexed by n (n = 1, 2) by Equation(7);
apply the Harris corner detector using Equation 10;
descriptor f(Ψ^{k,σ}(x, y)) is computed via AGH or SGH;
for each pixel f(Ψ^{k,σ}(x, y)) do
    compute the curvature ratio r by calculating Equation (14) between the features f_1 and f_2 at feature points p ∈ LF_1 and p_2 ∈ LF_2 in the two LFs
    if r < 0.75 then
        output [p_1, p_2] as matching between LF_1 and LF_2.
    end if
end for
```

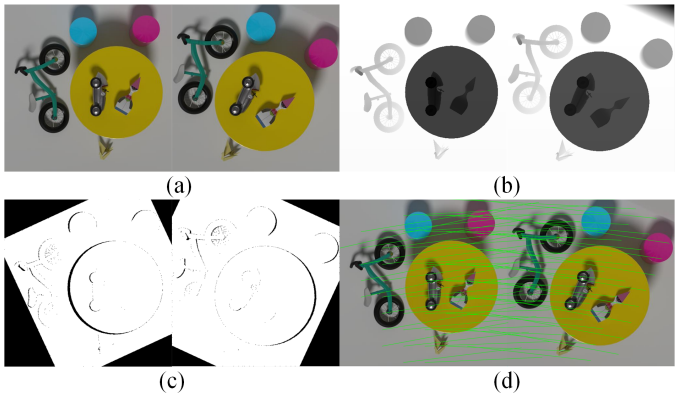

Fig. 7. Example of Blender synthetic LF matching dataset. (a) Central views of two LFs, with translation and rotation between the two; (b) Corresponding depth maps of (a); (c) Matching binary masks (black means that a matching point does not exist); (d) Pixel-wise matching ground truth of two LFs.

III. Feature Matching Dataset and Experiment

A. Synthetic dataset and real-world dataset

Given that no LF dataset is available with ground truth matching points, the authors in [15] evaluate their LiFF feature in the context of a SfM algorithm. We instead created a LF dataset with ground truth matching points using the open-source Blender [39] software. For each test data, we have generated a pair of LF images with known translation, rotation and camera settings. The LF includes $9 * 9$ views, each view is $512 * 512$ in spatial resolution, with a disparity range within the interval $[-2, 2]$ pixels.

The central views of a pair of LFs are shown in figure 7(a). Using Blender, we can do a pixel-wise cross-checking for the pairs of pixels with inconsistent parallax (*i.e.*the occluded pixels) (see figure 7(c)) and compute matching points (see figure 7(d)) using ground truth depth (figure 7(b)).

To test the robustness of the proposed light field descriptor, we also captured real-world LFs, using both a first generation and a Illum Lytro camera. We capture multiple pairs of real-world LFs, in which the illumination and noise are more complex. With the Lytro camera, one LF of each pair has $11 * 13$ views, and each view has a $378 * 328$ spatial resolution. With the Illum camera, the angular resolution and spatial resolution are $15 * 17$ and $541 * 434$ respectively. Due to the limited aperture (or angular baseline) the disparity range of all real-world dataset is within $[-2, 2]$ pixels. Although the ground truth matches are not available using the LF Lytro cameras, the matching results can still be evaluated by computing the epipolar constraint and checking homography of coplanar points, as shown in figure 8.

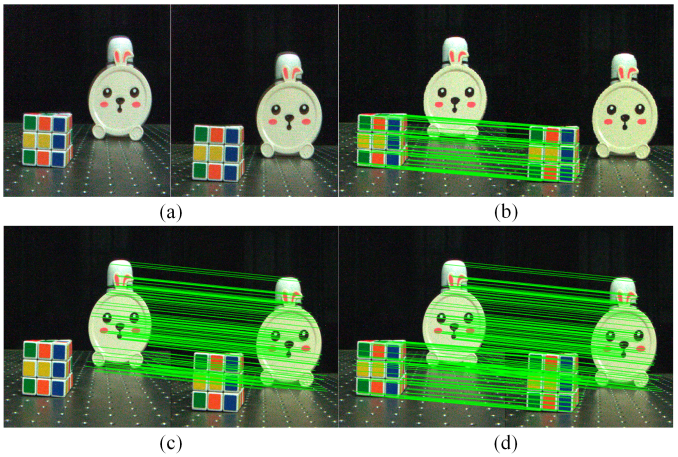

Fig. 8. Example of real-world LF matching dataset. (a) Central views of two LFs; (b) By calculating the homography of coplanar points, we obtain some reference matching points on a plane; (c) Reference matching point on another plane in the scene; (d) The union of reference matching points between the two LFs.

TABLE I
COMPARISON OF FEATURE MATCHING ON REAL-WORLD LFS(TOTAL MATCHES, MISMATCHES, PRECISION IN EACH GRID)

method	SIFT	LIFF	FDL-HSIFT	FDL-HAGH	FDL-HSGH
Book sewer	78	166	571	190	302
	12	22	50	10	28
	0.85	0.87	0.91	**0.95**	0.91
Bracket and plants	101	232	739	200	300
	11	28	43	5	17
	0.89	0.88	0.94	**0.98**	0.94
Plush toys	104	208	419	146	272
	7	20	31	4	8
	0.93	0.90	0.93	**0.97**	**0.97**
Bottled drinks	66	683	1945	1307	1731
	19	101	139	62	123
	0.71	0.85	0.93	**0.95**	0.93
stone arch bridge	184	757	418	787	1073
	10	30	10	17	21
	0.95	0.96	**0.98**	**0.98**	**0.98**
Two bicycles	89	534	238	328	791
	6	51	17	16	31
	0.93	0.90	0.93	0.95	**0.96**
Flowers	18	334	297	128	368
	3	70	22	30	18
	0.83	0.79	0.93	0.77	**0.95**

TABLE II
COMPARISON OF FEATURE MATCHING ON SYNTHETIC LFS (TOTAL NUMBER OF MATCHES, OF MISMATCHES, PRECISION, RECALL IN EACH GRID)

method	SIFT	LIFF	FDL-HSIFT	FDL-HAGH	FDL-HSGH
Bicycles	215	324	141	182	318
	15	21	2	5	8
	0.94	0.94	**0.99**	0.97	0.98
	0.10	**0.15**	0.07	0.09	**0.15**
Chess and shelf	45	106	166	79	216
	7	15	15	9	7
	0.87	0.88	0.92	0.90	**0.97**
	0.03	0.07	0.11	0.05	**0.14**
Office	59	89	157	42	76
	9	17	2	2	2
	0.87	0.84	**0.98**	0.96	0.97
	0.02	0.03	**0.06**	0.02	0.03

B. Evaluation on feature matching results

First, we evaluate the detection and matching performance of the two FDL-HAGH and FDL-HSGH variants of the proposed circular neighborhood FDL-HCGH descriptor, in comparison with the application of the SIFT feature descriptor [2] to the central views of the two light fields, and in comparison with LiFF [15] and the FDL-HSIFT descriptor [30]. Since pixel-wise matching ground truth is available with the synthetic LF dataset, we calculate both the precision and recall on the created synthetic LF dataset. However, the ground truth matching points of the real-world LF dataset are unknown, so we use homography matrix to check the matching correctness. Feature detection and matching results of each LF pair in figure 9, 11 are divided into three columns, the first and the third column give the feature detection results of the left and right LFs respectively, and the second column gives the matching results.

Figure 9, 10 and figure 11 are the feature detection and matching results on the real-world LF dataset and synthetic LF dataset, respectively. One can see visually that the features detected and matched by the proposed algorithm are more precise than the traditional SIFT and LiFF methods. Readers are encouraged to zoom in and to observe the false positive matches and true positive matches, which are marked as red lines and green lines respectively. In figure 10, the scenes are more complex and include objects with more continuous depth variation. According to the objective numerical results in Tab. I and Tab. II, the FDL-HCGH feature has higher precision than the other features on most real-world and synthetic LF dataset. From the numerical results, the precision of the proposed FDL-HCGH feature, i.e. of both FDL-HAGH and FDL-HSGH variants of the proposed FDL-HCGH, is significantly higher than that of the SIFT and LIFF features. In addition, the numerical results also show that the precision of the feature descriptor based on circular neighborhood is better than that based on square neighborhood in most cases. The AGH and SGH are comparable in percentage of true positive matches. Although sharing the same circular neighborhood, the AGH and SGH are sensitive to different variations, which are in radial direction and angular orientation respectively. The AGH usually has a shorter feature descriptor, while SGH generates more matching pairs. Unfortunately, the proposed algorithm will generate less matches in the presence of occlusion, *e.g.* please see the results of the $Flowers$ dataset in figure 10. For the $Flowers$ dataset, attentive readers will also find a significant performance drop with the AGH. According to our analysis, this is because the radial variations will be less perceivable after FDL decomposition, especially when the foreground object is similar to its background. Due to the trade-off problem between the matching precision and recall, a larger value of parameters K and a reasonable small value of r are suggested as handling scenes including complex textural objects within a large disparity range.

In order to verify the local invariance (such as translation, rotation and scale invariance) of FDL-HCGH feature, we use blender to make a synthetic LF dataset with only translation, or rotation, or scale transformation. The feature detecting and matching results are shown in figure 12, in which the translation, rotation and scale transformation are ideally using

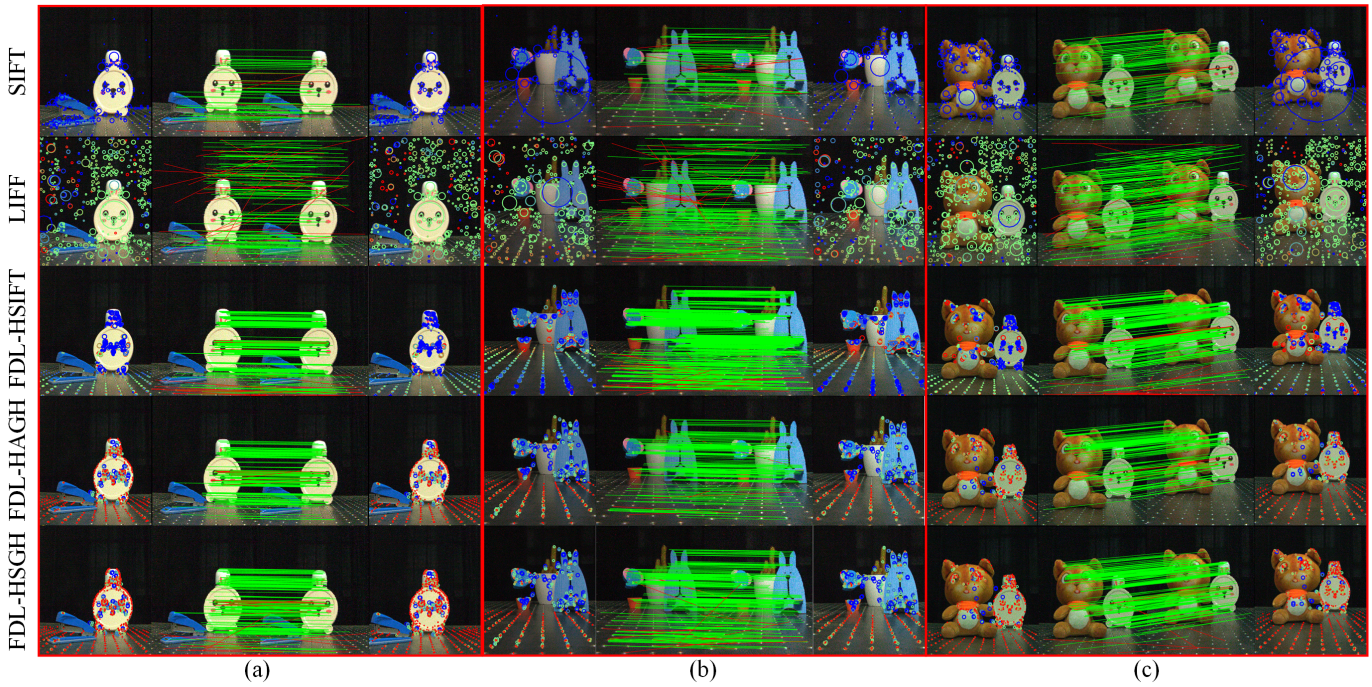

Fig. 9. Feature detection and matching results on real-world LFs. FDL-HAGH and FDL-HSGH are the two particular cases of the proposed FDL-HCGH, depending on the area on which the histograms of gradients are computed. For each dataset, the left and right columns show detection results, the middle column shows matching results. The size of the circle indicates the scale of the feature, and the color of the circle indicates that the feature is detected in different disparity layers.

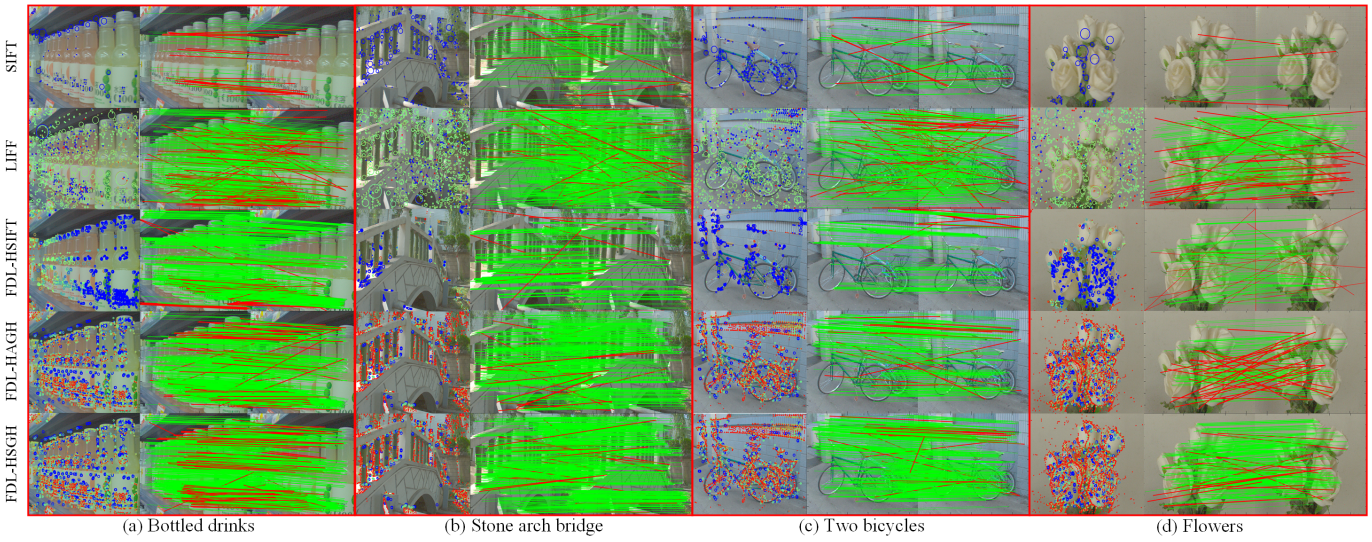

Fig. 10. Feature detection and matching results with extra real-world indoor and outdoor scenes, which include objects with more continuous depth variation.

Blender simulation. The pair of LFs are changed in scale in figure 12(a), are translated in figure 12(b), and are rotated in figure 12(c) respectively. Tab. III shows the comparison in terms of precision and recall of the feature matching. Both the visual matches representation and the numerical results show that the precision and recall of the FDL-HCGH feature (of both FDL-HAGH and FDL-HSGH variants of the proposed FDL-HCGH) are better than those obtained with the SIFT and LIFF features. Moreover, the precision and recall of the FDL-HCGH feature are better than the FDL-HSIFT feature based on a square neighborhood. This also shows that the CGH descriptor are more robust to translation, rotation and scale variation. So, the AGH and SGH feature descriptors based on circular neighborhood are robust to scale, translation and rotation variation, and the precision and recall of feature detection and matching are the best in most cases. Although the proposed algorithm can benefit from the non-Lambertian surfaces and occlusions handling capacity of the FDL representation, the matching process still relies heavily on the angular consistency of feature extraction. Besides, the angular covering capability of a LF camera will be relative decreased as increasing the baseline of a stereo LFs. Therefore, it is still challenging to deal with those pairs of LFs with a relative large translation, rotation and scale variation.

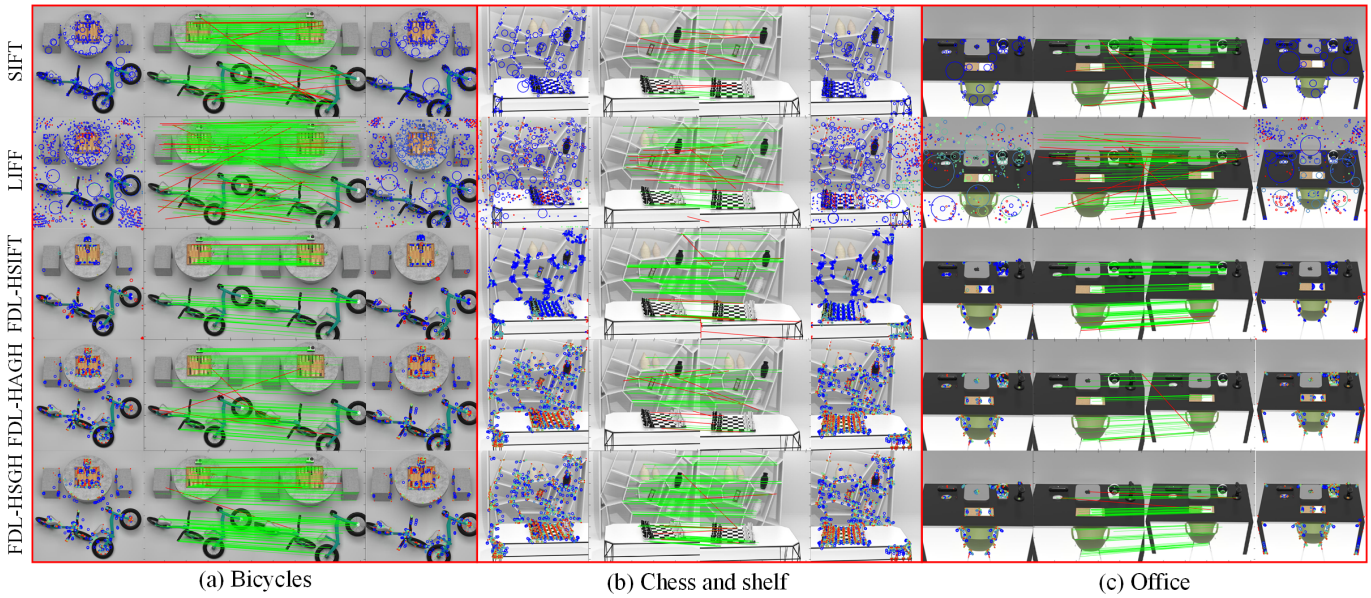

Fig. 11. Feature detection and matching results with synthetic LF pairs. FDL-HAGH and FDL-HSGH are the two particular cases of the proposed FDL-HCGH, depending on the area on which the histograms of gradients are computed. One can see that the proposed FDL-HCGH feature can generate more precise results in correspondences, *i.e.*a less percentage red lines, compared with the matching ground truth.

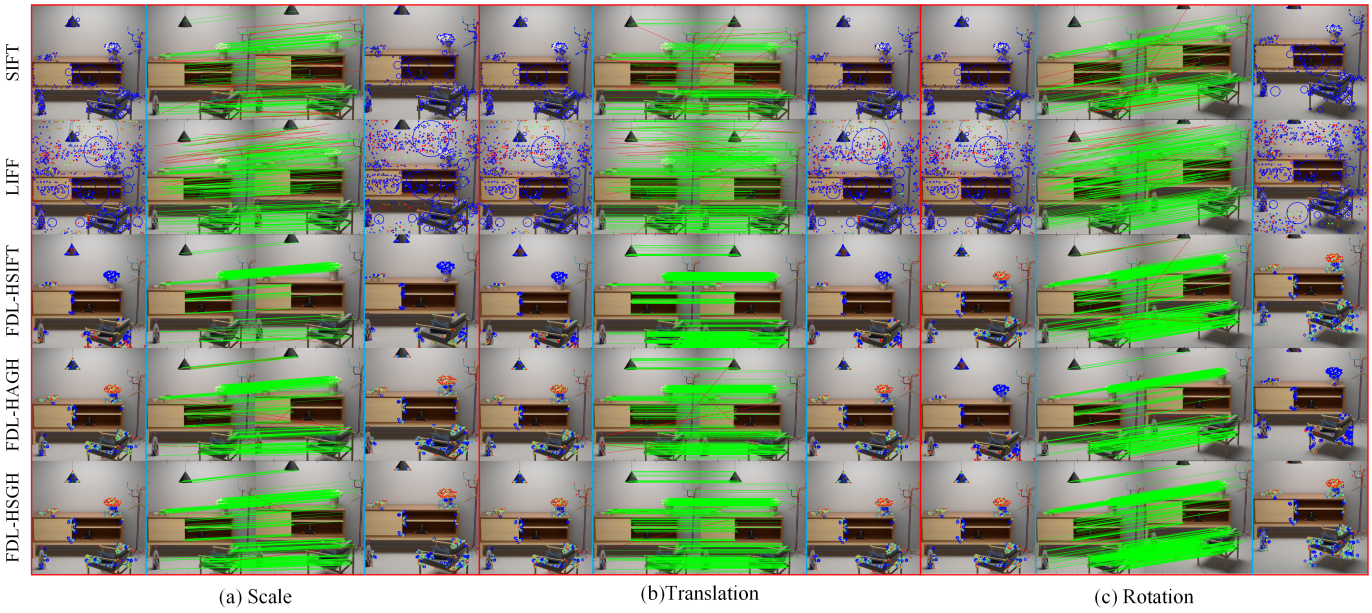

Fig. 12. Feature detection and matching results with synthetic LFs. (a) with scale transformation. (b) with translation. (c) with rotation.

C. Computational complexity

The runtime of the proposed FDL-HCGH feature matching method is divided into three parts: scale-disparity space construction, feature detection and description, and feature matching. let us assume a 4D $LF(x, y, u, v)$, which is constructed as a SDS $\Psi(x, y, k, \sigma)$. Comparing complexity, FDL-HCGH is at least $(u \times v)/k$ times faster than repeated SIFT. For LiFF descriptor, one question inherent is the discretization of the depth space, which has significant impact on computational complexity. The depth space discretization corresponds to a list of slopes, a higher number of slopes giving a better performance, but a higher computational complexity.

As for feature detection and description, LIFF descriptor is an extension of SIFT in the 4D space, and its computational complexity is the same. The proposed FDL-HCGH feature is a combination of Harris feature detection and circular gradient histogram description. Harris detection is more efficient than SIFT, while we also show that the CGH feature description method using circular neighborhood is more efficient than the SIFT feature descriptor using a square neighborhood.

For feature matching, the three methods are the same. On the whole, the computational complexity of the proposed FDL-HCGH feature is very low. Tab. IV give the runtime values for the the three methods using real-world and synthetic LF pairs. Experiment show that the computational complexity of the matching process using the FDL-HCGH feature is the lowest.

TABLE III
FEATURE MATCHING WITH SYNTHETIC LF PAIRS WITH ONLY TRANSLATION, ROTATION, OR SCALE TRANSFORMATION, USING DIFFERENT ALGORITHMS. (TOTAL NUMBER OF MATCHES, OF MISMATCHES, PRECISION, RECALL IN EACH GRID)

Transformation	SIFT	LIFF	FDL-HSIFT	FDL-HAGH	FDL-HSGH
Scale	149	238	224	262	384
	24	22	2	7	4
	0.86	0.91	**0.99**	0.97	**0.99**
	0.07	0.11	0.11	0.12	**0.18**
Translation	180	371	757	512	596
	22	23	6	10	2
	0.89	0.94	**0.99**	0.98	**0.99**
	0.037	0.15	**0.29**	0.20	0.24
Rotation	181	342	527	480	618
	17	18	8	10	1
	0.91	0.95	0.98	0.98	**0.99**
	0.08	0.15	0.24	0.22	**0.28**

TABLE IV
RUNTIME COMPARISON OF FEATURE DETECTION AND MATCHING ON DIFFERENT LFS.

runtime(s)	SIFT	LIFF	FDL-HSIFT	FDL-HAGH	FDL-HSGH
Book sewer	227.92	32.27	61.38	**23.25**	23.33
Bracket and plants	251.18	28.52	64.73	**20.53**	20.73
Plush toys	223.08	36.28	69.77	**21.24**	21.55
Bottled drinks	296.25	148.09	189.68	52.50	**48.51**
Stone arch bridge	396.03	152.57	93.49	62.22	**58.12**
Two bicycles	380.73	312.30	161.42	**51.93**	52.74
Flowers	231.68	115.61	103.80	70.33	**61.08**
Bicycles	379.13	84.82	58.92	44.35	**39.51**
Chess and shelf	433.97	92.31	119.58	**47.44**	51.03
Office	223.75	49.28	51.27	**30.61**	33.49
Locker(scale)	422.91	110.61	60.77	43.63	**39.37**
Loker(translation)	441.33	94.15	61.70	39.78	**39.58**
Locker(rotation)	435.53	69.72	61.91	**38.83**	39.65

Furthermore, in order to verify the efficiency of each part of the proposed AGH and SGH descriptor based matching methods, in addition to the construction of scale-disparity space, the algorithm can be divided into three parts: detection, description and matching. We therefore measure the average runtime of these three parts in different FDL disparity layers using both the real-world and synthetic LF dataset. Tab V, shows that the runtime values of each part of the AGH and SGH algorithms, which demonstrates the efficiency of our FDL-HCGH feature. Moreover, the runtime values obtained with the real-world LF dataset are lower than when using the synthetic LF dataset. The reason is that the spatial resolution of the synthetic LF (512 * 512) is larger than that of the real-world LF (378 * 328). In addition, we can see that with the increase of the number of FDL disparity layers, the runtime of each part of AGH and SGH methods basically increases by less than 2 seconds. Therefore, if the scene is complex and the number of FDL disparity layers needs to be increased, our AGH and SGH descriptors remain very efficient.

D. Limitations

The proposed FDL-HCGH feature matching still suffers from the trade-off between the matching precision and recall. The FDL-HCGH feature matching can be vulnerable when dealing with a pairs of LFs with a wide baseline, which leads to relative large translation, rotation, scale variation and severe occlusions. The matching process of FDL-HCGH still relies heavily on the angular consistency of feature extraction. Unfortunately, the angular covering capability of a LF camera may not be sufficient to handle scenes with Non-lambertian objects and a large disparity range. Besides, some important parameters have been empirically selected, *e.g.* the numbers of Fourier disparity layers K and the matching threshold r, thus potential applications will benefit from further study on adaptive selection or optimization of parameters K and r.

TABLE V
RUNTIME OF DETECTION, DESCRIPTION AND MATCHING OF AGH AND SGH METHODS ON DIFFERENT FDL DISPARITY LAYERS.

runtime(s)	layers	detection	description	matching
AGH (real-world)	5	1.78	2.64	1.97
	7	2.29	3.52	2.42
	9	2.65	4.38	2.81
SGH (real-world)	5	1.78	2.86	2.07
	7	2.24	3.76	2.52
	9	2.66	4.67	2.97
AGH (synthetic)	5	3.19	5.92	3.43
	7	4.28	7.18	3.87
	9	4.81	8.45	4.25
SGH (synthetic)	5	3.22	5.85	3.49
	7	4.39	7.03	3.86
	9	4.87	8.39	4.27

IV. CONCLUSION

In this paper, we propose a FDL-HCGH feature for 4D LF. To make the proposed feature robust to scale variance, based on the Fourier disparity layer representation, we construct a scale-disparity space, in which we perform Harris corner detection. In addition, in order to ensure rotation invariance and to reduce computational complexity, we propose a novel CGH feature descriptor using either annular gradient histograms or sector gradient histograms. The proposed descriptors are proved to be robust to translation, rotation and scale transformation. Moreover, we use the open-source software Blender to create a synthetic LF dataset with ground truth matching points, which enable to perform a better quantitative analysis. Experimental results show that the proposed feature has better precision and lower computational complexity compared to the state-of-the-art LiFF feature.

REFERENCES

[1] C. Harris, M. Stephens, *et al.*, "A combined corner and edge detector," in *Alvey Vision Conference*, vol. 15, pp. 10–5244, Citeseer, 1988.

[2] D. G. Lowe, "Distinctive image features from scale-invariant keypoints," *International Journal of Computer Vision*, vol. 60, no. 2, pp. 91–110, 2004.

[3] H. Bay, T. Tuytelaars, and L. Van Gool, "SURF: Speeded up robust features," in *European Conference on Computer Vision*, pp. 404–417, Springer, 2006.

[4] E. Rosten and T. Drummond, "Machine learning for high-speed corner detection," in *European Conference on Computer Vision*, pp. 430–443, Springer, 2006.

[5] E. Rublee, V. Rabaud, K. Konolige, and G. Bradski, "ORB: An efficient alternative to SIFT or SURF," in *2011 International Conference on Computer Vision*, pp. 2564–2571, IEEE, 2011.

[6] T. Ojala, M. Pietikäinen, and D. Harwood, "A comparative study of texture measures with classification based on featured distributions," *Pattern Recognition*, vol. 29, no. 1, pp. 51–59, 1996.

[7] Y. Ke and R. Sukthankar, "PCA-SIFT: A more distinctive representation for local image descriptors," in *IEEE Computer Society Conference on Computer Vision and Pattern Recognition*, vol. 2, pp. II–II, IEEE, 2004.

[8] K. Mikolajczyk and C. Schmid, "A performance evaluation of local descriptors," *IEEE Transactions on Pattern Analysis and Machine Intelligence*, vol. 27, no. 10, pp. 1615–1630, 2005.

[9] Y. Wu, "Research on feature point extraction and matching machine learning method based on light field imaging," *Neural Computing and Applications*, vol. 31, no. 12, pp. 8157–8169, 2019.

[10] C. Zhao, Z. Cao, J. Yang, K. Xian, and X. Li, "Image feature correspondence selection: A comparative study and a new contribution," *IEEE Transactions on Image Processing*, vol. 29, pp. 3506–3519, 2020.

[11] Y. Zhong, "Intrinsic shape signatures: A shape descriptor for 3D object recognition," in *IEEE International Conference on Computer Vision Workshops*, pp. 689–696, IEEE, 2009.

[12] S. Gupta, P. Arbelaez, and J. Malik, "Perceptual organization and recognition of indoor scenes from RGB-D images," in *IEEE Conference on Computer Vision and Pattern Recognition*, pp. 564–571, 2013.

[13] X. Gao and T. Zhang, "Robust RGB-D simultaneous localization and mapping using planar point features," *Robotics and Autonomous Systems*, vol. 72, pp. 1–14, 2015.

[14] I. Tošić and K. Berkner, "3D keypoint detection by light field scale-depth space analysis," in *2014 IEEE International Conference on Image Processing*, pp. 1927–1931, IEEE, 2014.

[15] D. G. Dansereau, B. Girod, and G. Wetzstein, "LiFF: Light field features in scale and depth," in *IEEE/CVF Conference on Computer Vision and Pattern Recognition*, pp. 8042–8051, 2019.

[16] Y. Rao, B. Fan, Q. Wang, J. Pu, X. Luo, and R. Jin, "Extreme feature regions detection and accurate quality assessment for point-cloud 3D reconstruction," *IEEE Access*, vol. 7, pp. 37757–37769, 2019.

[17] Y. Xian, J. Xiao, and Y. Wang, "A fast registration algorithm of rock point cloud based on spherical projection and feature extraction," *Frontiers of Computer Science*, vol. 13, no. 1, pp. 170–182, 2019.

[18] S. Gupta, R. Girshick, P. Arbeláez, and J. Malik, "Learning rich features from RGB-D images for object detection and segmentation," in *European Conference on Computer Vision*, pp. 345–360, Springer, 2014.

[19] A. Ghasemi and M. Vetterli, "Scale-invariant representation of light field images for object recognition and tracking," in *Computational Imaging XII*, vol. 9020, p. 902015, International Society for Optics and Photonics, 2014.

[20] J. A. Teixeira, C. Brites, F. Pereira, and J. Ascenso, "Epipolar based light field key-location detector," in *International Workshop on Multimedia Signal Processing*, pp. 1–6, 2017.

[21] O. Johannsen, A. Sulc, and B. Goldluecke, "On linear structure from motion for light field cameras," in *IEEE International Conference on Computer Vision*, pp. 720–728, 2015.

[22] K. Maeno, H. Nagahara, A. Shimada, and R.-i. Taniguchi, "Light field distortion feature for transparent object recognition," in *IEEE Conference on Computer Vision and Pattern Recognition*, pp. 2786–2793, 2013.

[23] Y. Xu, H. Nagahara, A. Shimada, and R.-i. Taniguchi, "Transcut: Transparent object segmentation from a light-field image," in *IEEE International Conference on Computer Vision*, pp. 3442–3450, 2015.

[24] R. Raghavendra, K. B. Raja, and C. Busch, "Presentation attack detection for face recognition using light field camera," *IEEE Transactions on Image Processing*, vol. 24, no. 3, pp. 1060–1075, 2015.

[25] D. Tsai, D. G. Dansereau, T. Peynot, and P. Corke, "Distinguishing refracted features using light field cameras with application to structure from motion," *IEEE Robotics and Automation Letters*, vol. 4, no. 2, pp. 177–184, 2018.

[26] Z. Ji, H. Zhu, and Q. Wang, "LFHOG: A discriminative descriptor for live face detection from light field image," in *2016 IEEE International Conference on Image Processing*, pp. 1474–1478, IEEE, 2016.

[27] A. Sepas-Moghaddam, P. L. Correia, and F. Pereira, "Light field local binary patterns description for face recognition," in *2017 IEEE International Conference on Image Processing*, pp. 3815–3819, IEEE, 2017.

[28] M. Alain and A. Smolic, "A spatio-angular binary descriptor for fast light field inter view matching," in *2020 IEEE International Conference on Image Processing*, pp. 2636–2640, IEEE, 2020.

[29] M. Le Pendu, C. Guillemot, and A. Smolic, "A fourier disparity layer representation for light fields," *IEEE Transactions on Image Processing*, vol. 28, no. 11, pp. 5740–5753, 2019.

[30] Z. Xiao, M. Zhang, H. Jin, and C. Guillemot, "A light field FDL-HSIFT feature in scale-disparity space," in *2021 IEEE International Conference on Image Processing (ICIP)*, pp. 1549–1553, 2021.

[31] B. Liu, H. Wu, W. Su, and J. Sun, "Sector-ring HOG for rotation-invariant human detection," *Signal Processing: Image Communication*, vol. 54, pp. 1–10, 2017.

[32] M. Levoy and P. Hanrahan, "Light field rendering," in *The 23rd Annual Conference on Computer Graphics and Interactive Techniques*, pp. 31–42, 1996.

[33] S. J. Gortler, R. Grzeszczuk, R. Szeliski, and M. F. Cohen, "The lumigraph," in *The 23rd Annual Conference on Computer Graphics and Interactive Techniques*, pp. 43–54, 1996.

[34] B. Wilburn, N. Joshi, V. Vaish, E.-V. Talvala, E. Antunez, A. Barth, A. Adams, M. Horowitz, and M. Levoy, "High performance imaging using large camera arrays," in *ACM SIGGRAPH 2005 Papers*, pp. 765–776, 2005.

[35] R. Ng, M. Levoy, M. Brédif, G. Duval, M. Horowitz, and P. Hanrahan, *Light field photography with a hand-held plenoptic camera*. PhD thesis, Stanford University, 2005.

[36] G. Wu, B. Masia, A. Jarabo, Y. Zhang, L. Wang, Q. Dai, T. Chai, and Y. Liu, "Light field image processing: An overview," *IEEE Journal of Selected Topics in Signal Processing*, vol. 11, no. 7, pp. 926–954, 2017.

[37] I. Ihrke, J. Restrepo, and L. Mignard-Debise, "Principles of light field imaging: Briefly revisiting 25 years of research," *IEEE Signal Processing Magazine*, vol. 33, no. 5, pp. 59–69, 2016.

[38] T. Lindeberg, *Scale-space theory in computer vision*, vol. 256. Springer Science & Business Media, 2013.

[39] K. Honauer, O. Johannsen, D. Kondermann, and B. Goldluecke, "A dataset and evaluation methodology for depth estimation on 4D light fields," in *Asian Conference on Computer Vision*, Springer, 2016.

Meng Zhang is currently a PhD student in the School of Computer Science and Engineering of Xi'an University of Technology. Her research interests are computational photography and computer vision.

Haiyan Jin is a Professor in Xi'an University of Technology, and head of a research team for Image and Vision Computing Group (IVCG). She holds a Ph.D. degree from Xidian University, China, in 2007. She presided more than ten projects including the National Natural Science Foundation of China, the Natural Science Basic Research Project of Shaanxi. Her research interests include computer vision, image processing and intelligent optimization. E-mail: jinhaiyan@xaut.edu.cn

Zhaolin Xiao is an Associate Professor in Xi'an University of Technology. He received a Ph.D. degree in computer science from Northwestern Polytechnical University, China, in 2014. From Dec. 2018 to 2019, He worked as a visiting scholar at INRIA in France. In 2012, He worked as a visiting student (overseas joint-training program) in the School of Computer Science, The University of Wisconsin-Madison. His research interests include computational photography, image processing, computer vision, and in particular light field imaging and processing. E-mail:xiaozhaolin@xaut.edu.cn

Christine Guillemot, IEEE fellow, is Director of Research at INRIA, head of a research team dealing with image and video modeling, processing, coding and communication. She holds a Ph.D. degree from ENST (Ecole Nationale Superieure des Telecommunications) Paris, and an Habilitation for Research Direction from the University of Rennes. From 1985 to Oct. 1997, she has been with FRANCE TELECOM, where she has been involved in various projects in the area of image and video coding for TV, HDTV and multimedia. From Jan. 1990 to mid 1991, she has worked at Bellcore, NJ, USA, as a visiting scientist. Her research interests are signal and image processing, and in particular 2D and 3D image and video processing for various problems (compression, super-resolution, inpainting, classification).

She has served as Associate Editor for IEEE Trans. on Image Processing (from 2000 to 2003, and from 2014-2016), for IEEE Trans. on Circuits and Systems for Video Technology (from 2004 to 2006), and for IEEE Trans. on Signal Processing (2007-2009). She has served as senior member of the editorial board of the IEEE journal on selected topics in signal processing (2013-2015) and is currently senior area editor of IEEE Trans. on Image Processing.